Small ZSM-5 crystals with low defect density as an effective catalyst for conversion of methanol to hydrocarbons

Small ZSM-5 crystals with low defect density as an effective catalyst for conversion of methanol to hydrocarbons

Mattias Grahn [a], Abrar Faisal [a†], Olov G. W. Öhrman [a,b], Ming Zhou[a], Matteo Signorile[c], Valentina Crocellà[c], Mohammad Sadegh Nabavi[a] and Jonas Hedlund[a]**

[a] Chemical Technology, Luleå University of Technology, SE-971 87 Luleå, Sweden

[b] RISE ETC - Energy Technology Center, SE-941 28 Piteå, Sweden

[c] Department of Chemistry, NIS and INSTM Reference Centre, Università di Torino, Via G. Quarello 15, I-10135 and Via P. Giuria 7, I-10125, Torino, Italy

[†] Current address: Department of Chemical Engineering, COMSATS University Islamabad, Lahore Campus, Lahore, Pakistan.

* To whom correspondence should be addressed: valentina.crocella@unito.it; tel.: +39 011 670 8384 or jonas.hedlund@ltu.se; tel.: +46 920 492105

Keywords: ZSM-5, defects, hydrocarbons, deactivation, MTH, IR spectroscopy, OH groups

Abstract

This work presents the synthesis of nearly defect-free ZSM-5 nanosized crystals, prepared in fluoride medium by seeding with silicalite-1. This material was carefully characterized and its catalytic performances in the methanol to hydrocarbons (MTH) reaction were assessed. Such fluoride-based material was compared to a reference ZSM-5, produced through a conventional alkaline synthesis but from the same seeding. Despite both the materials show closely identical morphology and they have a comparable acid site population, the catalyst prepared using the fluoride route showed significantly longer lifetime in MTH compared to the catalyst prepared using conventional synthesis at high pH. The slower deactivation for the samples prepared using the fluoride route was ascribed, thanks to a thorough *in situ* IR spectroscopy study, to its lower density of internal defects. According to the UV-Raman characterization of coke on the spent catalyst, the fluoride-based ZSM-5 catalyst produces less molecular coke species, most probably because of the absence of enlarged cavities/channels as due to the presence of internal defects. On the basis of these observations, the deactivation mechanism in the ZSM-5 synthesized by fluoride medium could be mostly related to the deposition of an external layer

of bulk coke, whereas in the alkali-synthesized catalyst an additional effect from molecular coke accumulating within the porous network accelerates the deactivation process.

1. Introduction

The world relies today heavily on petroleum as a source for the vast quantities of transportation fuels and petrochemicals demanded. However, at the current consumption rate, reserves of petroleum will only last for a few more decades, furthermore forcing to the exploitation of progressively lower quality feedstocks. In contrast, reserves of natural gas and coal (and, on a greener perspective, biomasses) are significantly larger, therefore there is an increasing interest in technologies for upgrading these resources into liquid fuels or chemicals. The main routes for upgrading natural gas or coal/biomass into liquid fuels and chemicals are *via* reforming and gasification to produce synthesis gas that is further processed to a wide range of products. An alternative route to produce liquid hydrocarbons is the methanol to gasoline (MTG) process, discovered in the 1970's by researchers at Mobil Oil, where methanol is converted to a synthetic gasoline product over a protonic zeolite catalyst [1,2]. Furthermore, by tuning the operating conditions and the catalyst, methanol can also be converted into light olefins, in the so called methanol to olefins (MTO) process. Both MTG and MTO processes have been implemented in a number of pilot and commercial plants [3–5].

One of the major challenges for zeolite catalysts in both MTG/MTO is the formation of coke on the catalyst particles with time during the reaction, which reduces the activity of the catalyst and requires its frequent reactivation by oxidation at high temperature [6–10]. Owing to the importance of minimizing coke formation in the MTH reactions, there is a significant effort to address this issue [10]. H-ZSM-5, mostly employed in MTG, is generally considered as a catalyst quite resistant to deactivation by coke formation. It is agreed that in ZSM-5 external coke (i.e. forming outside the micropore system) is mostly responsible for the loss in activity with time on stream [5,6].

A successful strategy for delaying the onset of coke induced deactivation is to design specific catalyst morphologies, such as mass transfer rates of reactants and products within the catalysts are enhanced, thus facilitating their removal prior further reactions leading to coke could take place. The mostly adopted synthetic strategies consist in: i) generating multiple levels of porosity within the zeolites (i.e. making them hierarchical); ii) reducing the particle size down to the nanometric range. Several methods have been proposed to produce hierarchical/nanosized zeolites [11]. These include sacrificial templating with organic compounds during the synthesis [12,13], the post-synthesis modification of the zeolite (e.g. acid leaching, steaming or desilication in alkaline media) [14–18] or the direct synthesis by adopting peculiar conditions [19]. These materials have been evaluated in various catalysis applications, including MTG/MTO: as an example, Bjørgen et al reported increased lifetime

and selectivity towards the gasoline range of hydrocarbons for a mesoporous catalyst prepared by desilication compared to a non-treated reference catalyst [18]. Such behavior has been rationalized in terms of altered acidity, formation of mesopores and shorter effective diffusion path [20].

However, coke formation on H-ZSM-5 has also been shown to correlate to the presence of internal defects, in the form of silanol nests, as formed when the zeolite synthesis is performed at alkaline pH [21–23]. The correlation between coke formation and the presence of internal silanol groups is well known, e.g. it has been observed in o-xylene isomerization over H-ZSM-5 [24,25]. More recent studies showed that a clear correlation between the presence of internal framework defects and deactivation by coke exists also in the MTG/MTO processes [26–28]. In view of the results linking deactivation by coke formation in ZSM-5 to the presence of internal framework defects as discussed above, another strategy to postponing the onset of deactivation by coking may be to minimize the formation of internal framework defects during the synthesis of the crystals. Again, different approaches have been proposed, such as the post-synthesis silylation of the materials [29], the introduction of atomically dispersed transition metal dopants (e.g. tungsten)[30,31] or to perform the zeolite synthesis in fluoride medium. Concerning the last method, the fluoride route enables zeolite synthesis at near neutral pH, thus minimizing the number of non-bridging $\equiv$SiOH defects and yielding crystals with fewer framework defects [32]. However, zeolites synthesized via the fluoride route show larger crystals than ones prepared at high pH, because of the slower nucleation and the faster growth in the fluoride medium. Although such large crystals are valuable for fundamental studies, they are less useful in real applications because of their inherent mass transfer limitations [33,34]. Nevertheless, Bleken et al prepared large ZSM-5 catalysts using the fluoride route and compared the performance to ZSM-5 catalysts prepared in different ways in OH^- media, showing that the catalysts synthesized in fluoride medium has both the highest C_3/C_2 selectivity and the lowest deactivation rate [35]. Recently, Qin et al reported an elegant way of preparing nanosized ZSM-5 catalyst (with b-axis thickness of 200 nm) in fluoride medium by using seeded growth [36]. The silicalite-1 crystals used as seeds were however prepared in OH^- medium. The catalyst therefore consists of a silicalite-1 core (presumably containing defects) and an outer shell of ZSM-5 prepared in fluoride medium, and weather the defects from the seeds propagates into the outer ZSM-5 shell or not is unclear. Nevertheless, the catalyst was evaluated for MTO and compared to a reference catalyst prepared in OH^- medium. Although the initial methanol conversion differed substantially for the two catalysts tested, the results indicated that the ZSM-5 prepared in fluoride medium shows better resistance to deactivation by coke formation. Some of us recently reported the first synthesis of small silicalite-1 crystals using a fluoride route [22], with a very low defect density. The crystals show a platelet like morphology and their thickness may be tailored by altering the synthesis conditions (but this is typically less than 30 nm).

In the present work, we report the preparation of "defect free" (i.e. crystals with a very low defect density, since completely defect free crystals are probably impossible to achieve) ZSM-5 by fluoride route, using defect free silicalite-1 seed crystals for the first time. The obtained ZSM-5 shows crystals significantly thinner than previously reported. The samples were thoroughly characterized by means of powder XRD, SEM, N_2 physisorption at 77 K and IR spectroscopy, the latter augmented by probe molecules in order to fully assess the speciation and the distribution of the active acidic sites and the SiOH groups in the framework. In particular, carbon monoxide (CO) has been employed as a probe to qualitatively discriminate between sites of slightly different acidity, whereas pyridine adsorption has been performed to obtain quantitative information about the relative amounts of Brønsted and Lewis acid sites. Finally, adsorption of 2,4,6-trimethylpyridine (collidine), too bulky to diffuse into the ZSM-5 micropores, was used to study the accessibility and the location of the weak acidic SiOH sites, thus obtaining indirect information on the amount of defects present in samples synthesized following different routes. A ZSM-5 catalyst prepared in conventional OH^- medium was characterized as reference catalysts as well. The prepared crystals were also tested for conversion of methanol to hydrocarbons and the results in terms of initial selectivity and deactivation were compared. Finally, the materials were characterized by UV-Raman spectroscopy after the catalytic tests, thus highlighting the difference in the nature of the coke species responsible for the catalysts deactivation.

2. Experimental

2.1. Synthesis of silicalite-1(F) seeds

The detailed synthesis procedures of silicalite-1(F) seeds were reported previously[22] and it will be described in brief here. At first, clear synthesis solution was prepared by mixing and shaking tetraethoxysilane (TEOS, >98 %, Merck) and tetrapropylammonium hydroxide (TPAOH, 40 %, Sigma) for 24 h. Then, water and all ethanol were removed from the solution using a rotary evaporator operated at 50 °C for about 1 h, after which a solid like transparent gel was obtained. A certain amount of distilled water was added to the gel, after shaking several hours a clear viscous solution was obtained. The clear solution was placed in a polypropylene bottle with closed lid and heated at 60 °C for 6 days. Thereafter, hydrofluoric acid (38-40 wt. %, Merck) equal to the molar amount of TPAOH was quickly added to the viscous solution at 4 °C under stirring and after about 10 s, a clear gel with very high viscosity formed. The pH of this gel was 6.3. The resulting molar ratio of the clear gel was 0.36 TPAF : 1 SiO_2: 12 H_2O. Finally, the obtained gel was kept at 60 °C for 5 days for crystallization. The obtained silicalite-1(F) seeds were washed by centrifugation and dispersion in DDI water for 4 times, and then the seeds were dispersed in DDI water to form a suspension with seed concentration of 6 wt% before use.

2.2 Seeded growth of ZSM-5(F) from silicalite-1(F) seeds

ZSM-5(F) crystals with thicknesses of ca 100 nm were produced by seeded growth of silicalite-1(F) seed in a gel with a Si/Al ratio of 30 under hydrothermal treatment. Tetraethylammonium ion originating from tetraethylammonium hydroxide (TEAOH, 35 %, Sigma) was used as template. TEOS, aluminium isopropoxide, TEAOH and water were mixed, and hydrolysed for 24 h. Therafter 600 ppm silicalite-1(F) seed crystals were added to the clear solution. The suspension was followed by vigorous shaking for 1 h, and then cooled to 4 °C. In the next step, HF equal to TEAOH mole amount was quickly added into the suspension under stirring. After about 10 s, a solid like white gel formed. The molar composition of the gel was 12 TEAF : 25 SiO_2 : 0.417 Al_2O_3 : 500 H_2O : 2.5 i-PrOH : 100 EtOH (the seed crystals are omitted). This gel was hydrothermally treated at 175 °C for 48 h in a Teflon lined autoclave. The ZSM-5(F) crystals prepared in high yield were recovered by centrifugation and dispersion in distilled water for 4 times and freeze-dried.

2.3 Synthesis of ZSM-5(OH) reference crystals in hydroxide medium

ZSM-5(OH) crystals were prepared by adding 3.3 % silicalite-1(F) seeds to a gel with the composition 12 TEAOH : 25 SiO_2 : 0.4166 Al_2O_3 : 500 H_2O : 2.5 i-PrOH : 100 EtOH. After adding the seeds, the dispersion was homogenized by shaking for 1 h, and subsequently hydrothermally treated in an autoclave at 180 °C for 4 days. The yield of crystals was not very high, and after synthesis, the crystals were recovered by centrifugation at reduced speed resulting in an acceleration of about 22000 g followed by dispersion in distilled water 6 times and thereafter freeze dried. Centrifugation was carried out at reduced speed to separate the crystals from amorphous material.

2.4 Ion-exchange of the ZSM-5 catalysts

The as-synthesized ZSM-5 powders were first calcined at 823 K in air for 6 h. Thereafter, 5 g of powder was mixed with 80 g of a 10 wt.% NH_4NO_3 solution at 373 K for 1h. The powder was separated by centrifugation at 15000 g for 10 minutes followed by redispersion in fresh NH_4NO_3 solution under stirring, the procedure was repeated twice.

2.5 Characterization

Scanning electron microscopy (SEM) images were recorded on a FEI Magellan 400 field emission instrument without coating the samples.

X-ray powder diffraction (XRD) pattern were recorded using a Panalytical Empyrean diffractometer run in Bragg-Brentano geometry.

N_2 physisorption isoterms were recorded at 77 K on a Micromeritics ASAP 2010 instrument. Prior to measurements, the samples were outgassed at 623 K under vacuum for 10 h. The specific surface area (SSA) of each sample has been evaluated through both the Langmuir and the Brunauer-Emmett-Teller (BET) models. The micropores volume has been evaluated through the density functional theory (DFT) model, applied on the adsorption branch by assuming cylindrical-shaped pores.

Inductively coupled plasma – sector field mass spectrometry (ICP-SFMS, ALS Analytica) was exploited to determine the Si/Al ratios of the samples.

IR spectra were collected in transmission mode on a Bruker Vertex 70 Fourier transform spectrophotometer, equipped with a MCT cryodetector, accumulating 32 scans at 2 cm^{-1} resolution, at "beam temperature", i.e. the temperature reached by samples under the IR beam (around 323 K). The samples were examined in the form of self-supporting pellets mechanically protected with a pure gold envelope. Before each measurement, all samples were activated in controlled atmosphere following this activation procedure: each sample was heated up to 773 K with a ramp of 5 K/min under vacuum (< 10^{-3} mbar); after 1 h of outgassing at 773 K, 50 mbar of pure O_2 were dosed in the cell and left in contact for 1 h in order to oxidize the residuals of organic pollutants, using a home-made quartz IR cell, equipped with KBr windows and characterized by a very small optical path (ca. 2 mm) [37]. After the sample activation, the cell was connected to a conventional high-vacuum glass line, equipped with mechanical and turbo molecular pumps (capable of a residual pressure p < 10^{-3} mbar), that allows in situ adsorption/desorption measurements of the employed molecular probes. A special home-made quartz cell was used for operations down to liquid N_2 temperature (i.e. a nominal temperature of 77 K).

The materials were characterized employing as probe molecules CO, pyridine and 2,4,6-trimethylpyridine (collidine). The differences in acid strength and distribution of the different species were derived from the changes in IR absorption of CO adsorbed at 77 K on activated materials, reaching an ultimate equilibrium pressure of 70 mbar. Adsorption of pyridine and collidine was also performed by exposing the pellets to the vapor pressure of the respective compounds at beam temperature after activation.

The number of sites titrated by pyridine on self-supporting pellets was estimated from integrated IR peak areas of the analytical 19b vibrational modes of pyridine adsorbed on strong Brønsted Acid Sites (BAS), band at 1545 cm^{-1}, and Lewis Acid Sites (LAS), band at 1455 cm^{-1} [38]. The spectra used to evaluate the integrated areas were collected after contact of the activated samples with pyridine vapors, followed by evacuation at 473 K for 1 h to remove all the weakly physisorbed species. The concentration of acid sites referred to the unit weight of sample has been computed according to the following equations:

$$BAS(\mu mol/g) = \frac{A_{1545}(cm^{-1})}{\varepsilon_{BAS}(cm/\mu mol)} \cdot \frac{S(cm^2)}{w(g)} \qquad (1)$$

$$LAS(^{\mu mol}/_{g}) = \frac{A_{1455}(cm^{-1})}{\varepsilon_{LAS}(^{cm}/_{\mu mol})} \cdot \frac{S(cm^{2})}{w(g)} \qquad (2)$$

where A_{1545} and A_{1455} are the integrated areas of the 1545 and 1455 cm^{-1} signals, obtained by the spectra recorded after pyridine adsorption and evacuation at 473 K for 1h, ε_{BAS} and ε_{LAS} represent the integrated molar extinction coefficients of the aforementioned bands (the value reported by Emeis et al. [39] were exploited) and *S* and *w* are the geometrical area and the weight of the sample pellet respectively.

The band deconvolution of the IR spectra was carried out using the FIT routine by Bruker, which allows the interactive research of the best-fit to the examined experimental spectral segment on the basis of a number of spectral components imposed by the operator. All the major spectral parameters (spectral position, half-bandwidth, percent of Gaussian profile) were allowed floating freely.

UV-Raman spectra on spent catalysts were collected with a Renishaw inVia Raman Microscope spectrometer, coupled with a Coherent MotoFred 300C frequency doubled Ar^{+} laser emitting at 244 nm. The spectrometer works in backscattering mode and a 15x objective was exploited to convey the excitation beam on the sample and then to recollect the scattered light. The signal (upon filtering of the elastic scattering peak over a dielectric edge filter) was analyzed by a 3600 lines/mm grating and finally collected over a Peltier cooled CCD detector. Special care was put in avoiding the possible sample damaging, often occurring with high energy excitation sources: a specifically developed home-made setup was exploited for this purpose [40].

2.6 Evaluation of catalytic performance by conversion of methanol to hydrocarbons (MTH)

The catalyst tests were performed in a packed bed reactor operating at atmospheric pressure. The catalyst samples were mixed with milled sand in the ratio 1:50 and appropriate amounts of the catalyst/sand mixture were loaded into a stainless-steel reactor with an inner diameter of 20 mm and total length of 250 mm to give a total catalyst load in the reactor of 0.4 gram to arrive at a weight hourly space velocity (WHSV) of 2 $g_{methanol}\ g^{-1}_{catalyst}\ h^{-1}$. Crushed quartz glass and quartz glass wool were placed below and on top of the catalyst bed and a thermocouple was placed in the center of the catalyst bed to monitor the temperature. Nitrogen gas was saturated with methanol vapor at 291 K and fed to the reactor to obtain the desired WHSV. The flow of nitrogen to the saturator was controlled by a digital mass flow controller whereas the temperature of the saturator was controlled by a thermostat bath. Prior to the catalytic experiments, the loaded sample was activated by heating the reactor to 673 K for three hours under a flow of synthetic air, the catalytic experiments were conducted at 673 K. The reactor effluent was analyzed by an on-line gas chromatograph (Agilent 7890B) equipped with a FID detector and a capillary column (CP-Sil PONA CB fused silica WCOT). Sampling was performed

once every hour. The methanol conversion was calculated based on the difference in measured methanol concentrations C between reactor inlet and outlet as follows:

$$X_{MeOH}(\%) = \frac{C_{MeOH}^{in} - C_{MeOH}^{out}}{C_{MeOH}^{in}} \qquad (3)$$

3. Results and discussion

3.1. Characterization

3.1.1 Textural and morphological properties

The XRD data (Figure 1) of the synthesized crystals after calcination confirmed that all samples were highly crystalline MFI phase. Only reflections from the MFI phase is observed. No broad signals from amorphous material or any reflections from other phases are observed for both ZSM-5(F) and ZSM-5(OH) samples.

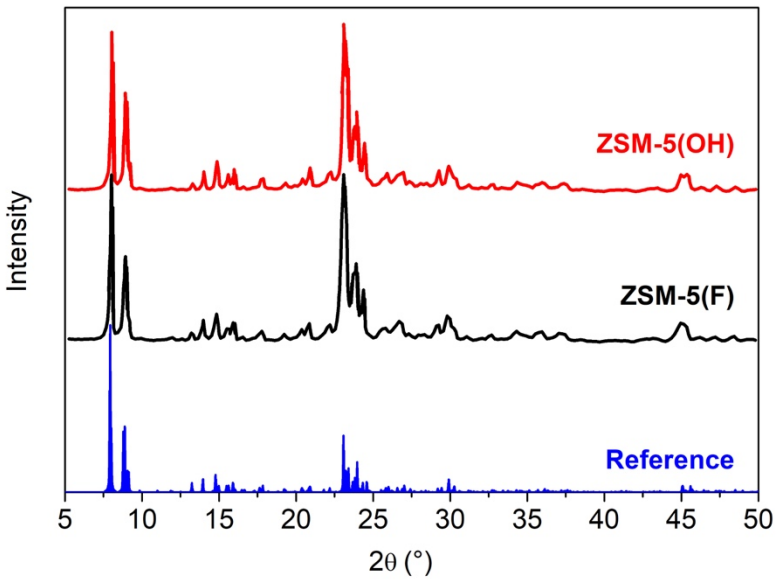

Figure 1. X-ray powder diffraction patterns of ZSM-5(F) (black) and ZSM-5(OH) (red) samples, compared to a reference pattern for the MFI topology (blue) [41].

Figure 2 shows the SEM image of the silicalite-1 seed crystals and of the two ZSM-5 catalyst prepared in fluoride and alkaline medium.

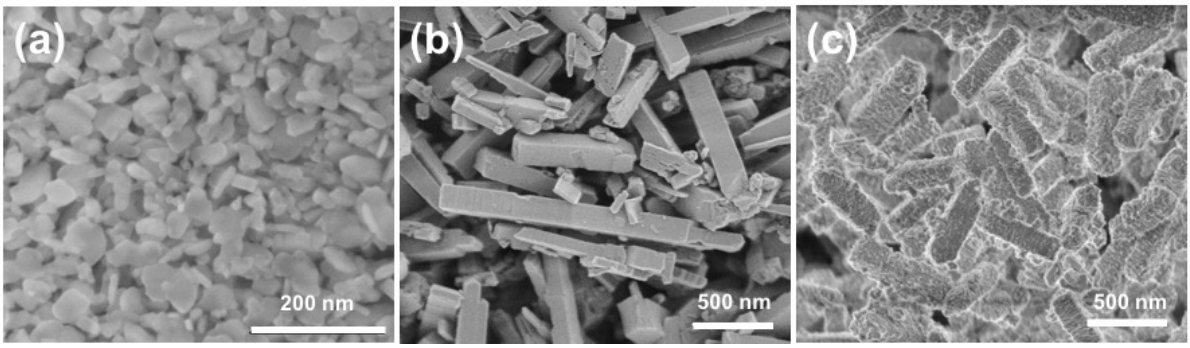

Figure 1. SEM images of (a) silicalite-1(F) seed crystals; (b) ZSM-5(F) crystals; and (c) ZSM-5(OH) crystals.

The silicalite-1(F) seeds are morphologically platelets with a radius of approximately 50 nm and a thickness of ca 10 nm. The SEM images of samples of ZSM-5(F) and ZSM-5(OH) show a change of morphology upon crystallization, leading for both the synthetic strategies to elongated parallelepiped crystals, having a thickness of ca 100 nm and variable length in the (sub)micrometric scale.

Despite the similar morphology, the Si/Al ratios for the two catalysts as determined by ICP-SFMS are quite different: 35.9 for ZSM-5(F) and 56.5 for ZSM-5(OH), respectively. The higher Si/Al ratio of the latter can be rationalized in terms of a larger addition of silicalite-1(F) seeds for its synthesis.

Figure 3 shows the N_2 adsorption/desorption isotherms at 77 K for the two samples. The isotherms exhibit the type I shape typical of microporous materials, with a steep increase in the amount adsorbed at low relative pressures.

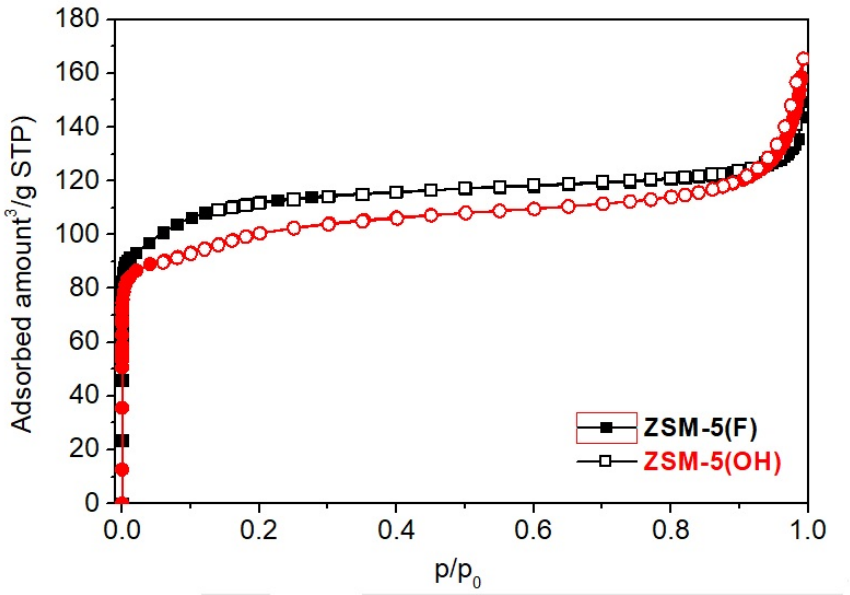

Figure 3. N_2 adsorption/desorption isotherms for the ZSM-5(F) (black squares) and ZSM-5(OH) (red circles) samples collected at 77K. The adsorption and the desorption branches are reported by full and empty symbols respectively.

The specific surface areas and the micropore volumes for the two samples are summarized in Table 1.

Table 1. Specific surface areas and micropore volumes for the two catalysts.

	BET SSA (m^2/g)	Langmuir SSA (m^2/g)	V_{micro}[a] (cm^3/g)
ZSM-5(F)	385	513	0.21
ZSM-5(OH)	344	461	0.16

[a] Calculated through DFT model, on the adsorption branch by assuming cylindrical-shaped pores.

Both the materials present SSA with similar magnitude, regardless the adopted model, in line with the expected values for zeolites with MFI topology [42]. The SSA values are just slightly lower in the case of ZSM-5(OH). The micropores volume shows both the materials are highly microporous, however following the same decreasing trend as for the SSA in the case of the alkali-synthesized sample.

3.1.2 Investigation of the acid sites: IR spectroscopy of adsorbed probe molecules

In situ IR spectroscopic measurements have been carried out on samples ZSM-5(F) and ZSM-5(OH) to obtain information about the amount, location and strength of the catalysts acid sites. The IR spectra of the two dehydrated catalysts in the OH stretching region are reported in Figure 4. After normalization to the zeolite overtone modes, the OH spectral profiles prove the different hydroxyl population of the two materials. The complex envelope of bands in the 3800-3100 cm^{-1} spectral range is ascribable to the presence of different families of OH groups (both isolated and interacting) located on the external and internal surface of the ZSM-5 materials.

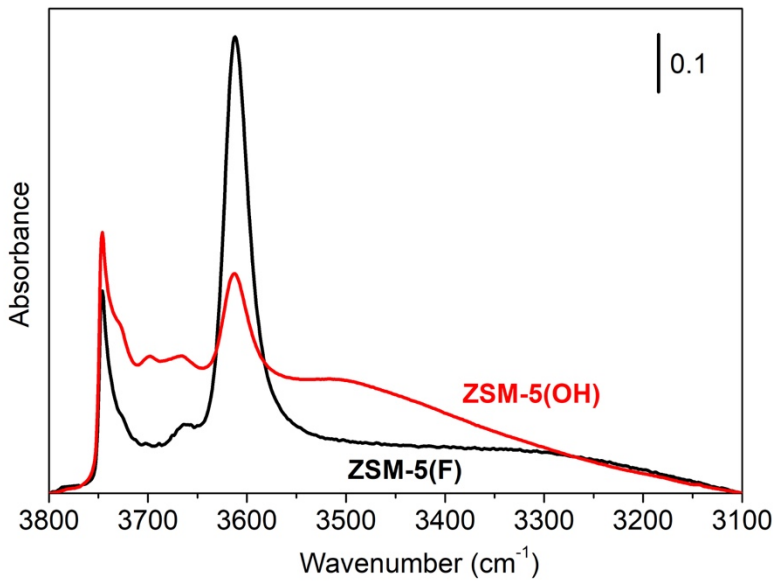

Figure 4. IR spectra in the OH stretching region, normalized to the zeolite overtone modes, of the catalysts activated at 500°C: ZSM-5(F) (black) and ZSM-5(OH) (red).

Considering the well-established literature on this topic [43], it is possible to unambiguously identify the different components present in the 3800-3100 cm^{-1} spectral range. The sharp and well-defined band at 3745 cm^{-1} is generated by virtually isolated SiOH groups located on the external surface of the zeolite, whereas the signals in the 3740-3700 cm^{-1} range can be assigned to weakly perturbed SiOH sites predominantly located inside the zeolite structure in terminal position in hydrogen-bonded silanols chains generated by the presence of defects (i.e. nanovoids generated by silicon vacancies). The broad and unresolved band with apparent maximum at around 3500 cm^{-1} (more evident in the case of the ZSM-5(OH) catalyst) is the spectral feature which testifies the presence of these internal cavities (defects) containing adjacent OH groups mutually interacting via medium-strength hydrogen bonds. Finally, the band representing the bridging strongly acidic Al(OH)Si Brønsted sites is located at around 3610 cm^{-1} and it is clearly more intense in the case of the ZSM-5(F) sample. Finally, a component at 3664 cm^{-1} ascribed to extra-framework AlOH species, testifying the presence of Lewis acid sites [44], is present in both samples. The possible AlOH groups give rise to a weak band at 3780 cm^{-1} as well: this signal is slightly visible in the case of ZSM-5(F) zeolite [45].

After this analysis, we can preliminary state that the two materials are characterized by a very different hydroxyl population and, in particular, that the ZSM-5(OH) catalyst likely possesses a higher number of hydroxylated cavities. A more extensive spectroscopic study with the use of specific probe molecules is now essential to evaluate the amount, the strength and the actual location (internal or external) of the various acid sites.

At first, we performed adsorption of carbon monoxide (CO) at the liquid nitrogen temperature (nominally 77 K), exploiting its subtle ability to discriminate between sites of slightly different acidity.

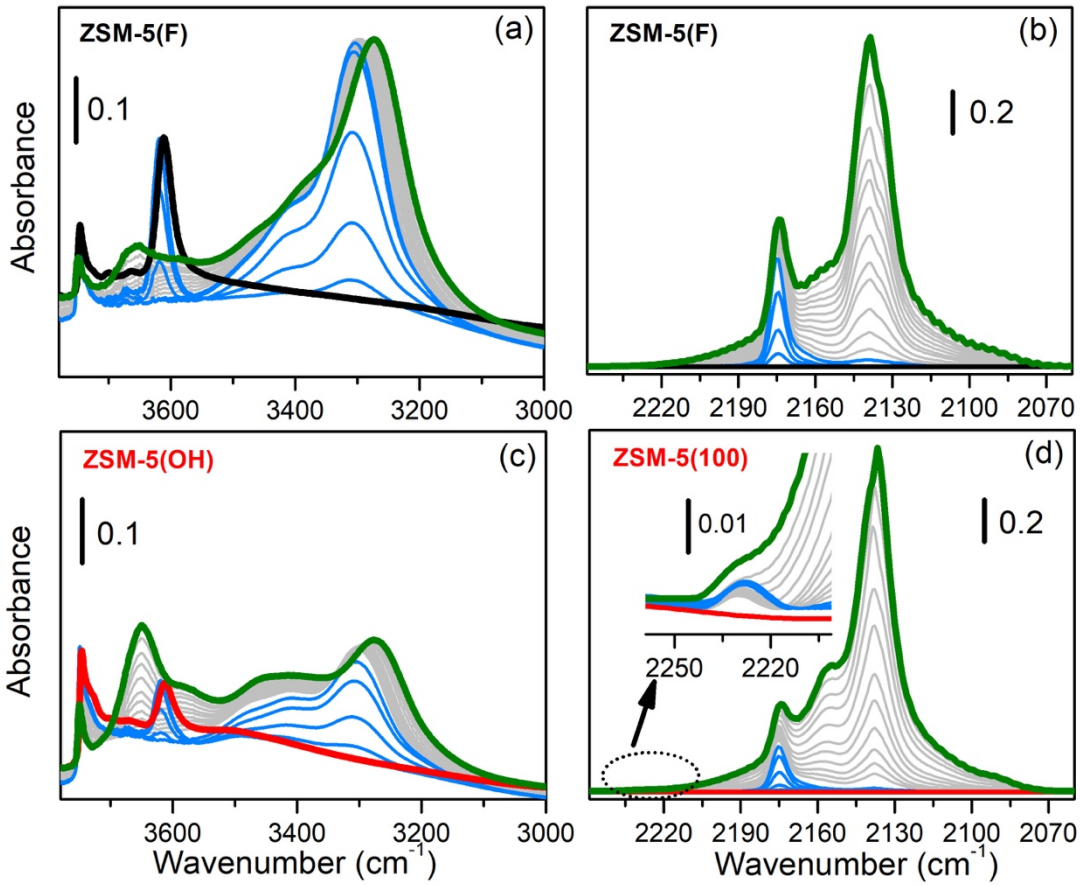

Figure 5. IR spectra of CO adsorption at 77 K at increasing coverage on activated ZSM-5(F) (sections (a) and (b)) and on activated ZSM-5(OH) (sections (c) and (d)). Sections (a) and (c) report the spectra in the OH stretching range and sections (b) and (d) show the CO vibrational modes region. Black spectra: ZSM-5(F) activated at 500°C. Red spectra: ZSM-5(OH) activated at 773 K. Green spectra: highest CO coverage (70 mbar). Light blue spectra: lowest CO coverages. Light gray spectra: intermediate adsorption steps. The inset of section (d) reports a magnification of the 2260-2200 cm^{-1} spectral range.

Figure 5 shows the CO adsorption spectra collected at 77 K on the considered materials after activation at 773 K. For what concerns the OH stretching region (Figure 5a and 5c), it can be observed that the signal generated by the strong Brønsted acid sites at 3610 cm^{-1} is consumed first and red-shifted to 3300 cm^{-1} (see light blue spectra), as usually observed in the case of H-ZSM-5 materials [46]. At low CO coverage, a broad component at around 3450 cm^{-1} also appears. This signal is ascribed to the perturbed OH groups of extra-framework Al originally absorbing at 3664 cm^{-1} [47]. By gradually increasing the CO coverage, the OH stretching vibrations of the weakly acidic SiOH components located at higher frequencies (3750-3700 cm^{-1}) are consumed and, at the same time, a broad envelope of bands with apparent maxima at around 3650 and 3570 cm^{-1} becomes evident (see light gray and green spectra). At the highest CO pressures (light grey - green spectra), the band of

perturbed Brønsted acid sites at 3300 cm^{-1} progressively shifts to 3270 cm^{-1} due to the multilayered CO adsorption [48]. The differences visible in the OH spectral profiles after the interaction with CO (i.e. the different intensity ratios among the perturbed OH bands) further prove that the two catalysts exhibit a dissimilar distribution of acidic sites.

Figure 5b and 5d display the CO vibrational modes region of ZSM-5(F) and ZSM-5(OH) respectively. At low CO coverage, a component at 2174 cm^{-1} appears in both samples due to the formation of CO adducts with the Brønsted acid sites. An upward shift of the CO stretching mode of +31 cm^{-1} with respect to the free gaseous molecule (2143 cm^{-1}) confirms the expected strong polarization of CO by the Brønsted acidic sites. The blue-shift of the ν_{CO} vibration is identical for the two samples due to the very similar acid strength of these species. By increasing the CO pressure, a broad signal at around 2150 cm^{-1} is also observed and assigned to CO interacting with the various SiOH groups (both internal and external). Finally, the strong signal at 2137 cm^{-1} grows in intensity when the liquid-like phase forms inside the zeolite micropores at the highest CO pressures [43]. In the case of the material synthesized in alkaline conditions, a rather weak component at 2230 cm^{-1}, only barely visible upon magnification (see inset of Figure 5d), is also present. This band is commonly attributed to CO adsorbed on strong Lewis acidic sites, generated by extra-framework Al species. This band is weak, but it should be kept in mind that the extinction coefficient of CO has been suggested to be diminished by the adsorption on Lewis sites if compared to the adsorption on Brønsted acidic species. The ratio between the two molar extinction coefficients ($\varepsilon(CO_{Lewis})/\varepsilon(CO_{Brønsted})$) has been reported to be as high as 0.32 [49], therefore the concentration of Lewis acid species could be not negligible with respect to the concentration of the Brønsted ones.

The CO adsorption provided an overview of the different acid sites present in the materials, also in the presence of rather small differences in acid strength. Pyridine, with its high proton affinity (930 kJ mol^{-1}) undergoes an immediate protonation in the presence of Brønsted acid sites and, in parallel, it can also be strongly adsorbed by Lewis acid sites, giving rise to peculiar vibrational features. For this reason, this molecular probe allows a quantitative determination of the two types of acid sites. In parallel, the use of a sterically hindered probe molecule like 2,4,6-trimethylpyridine (collidine), gives important information about the location of the different acid sites, among which the SiOH groups. This strong basic probe is too large to access the 10-membered rings proper of MFI topology and, therefore, can only interact with the acid sites fraction present at the external surface of the material.

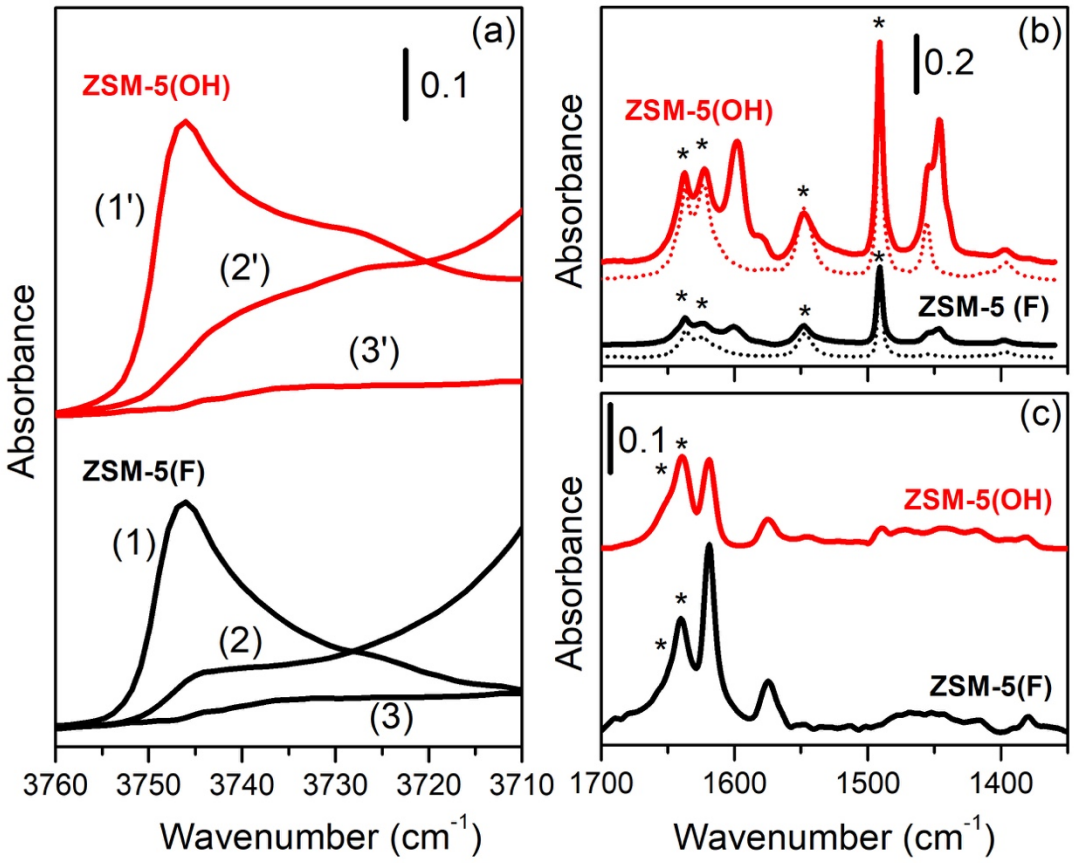

Figure 6. IR spectra of pyridine and collidine adsorption on activated ZSM-5(F) (black curves) and ZSM-5(OH) (red curves). Sections (a) reports the spectra in the weak acidic OH group stretching range, normalized to the zeolite overtone modes, after activation of the materials at 773 K (curves 1 and 1'), after interaction with collidine (curves 2 and 2') and pyridine (curves 3 and 3') vapor pressure. Sections (b) and (c) show the differential spectra (to which the spectrum of the activated solid has been subtracted) in the pyridine and collidine ring modes region respectively, collected after contact with the probe molecule and following long evacuation at room temperature for 2 h (solid curves) or evacuation at 473 K for 1h (dotted curves). Bands marked with an asterisk are assigned to protonated species. Differential spectra in section (b) and (c) have not been normalized to the samples thickness.

Figure 6a shows the spectra, in the weak acidic OH group stretching range, of ZSM-5(F) (black curves) and ZSM-5(OH) (red curves) samples after activation at 773 K (curves 1 and 1', respectively) and after interaction with collidine (curves 2 and 2', respectively) and pyridine (curves 3 and 3', respectively) vapor pressure. The adsorption of pyridine causes an almost total erosion of both unperturbed (isolated - mainly external) and weakly perturbed (terminals – mainly internal) hydroxyl groups signals (see spectra 3 and 3'). This probe, in fact, is able to enter the micropores of the ZSM-5 zeolite, thanks to its sufficiently low molecular diameter (5.7 Å). On the other hand, the adsorption of the sterically hindered collidine (with a diameter of 7.4 Å) is only responsible for the strong reduction

of the band at 3745 cm^{-1}, ascribed to isolated SiOH groups (usually located on the external surface of the zeolite). Instead, the bands of terminals SiOH species at lower frequencies (mainly associated with hydrogen-bonded silanols chains present in the defects) appear just partially attenuated by the interaction of collidine, proving that a consistent fraction of these silanols are located inside the micropores of the zeolite and, therefore, are not accessible to this larger probe molecule.

Figure 6b and 6c report the ring vibrational modes of the irreversibly adsorbed fraction of pyridine and collidine, i.e. after long evacuation at room temperature. The spectral features of protonated pyridine are well evident (see asterisks) in the spectra of the two samples (see Figure 6b) [27]. The bands evident at 1455 cm^{-1} can be instead assigned to the *19b* vibrational mode of pyridine interacting with strong Lewis sites (possible extra-framework Al species) [50].

As concerning collidine, the signals of protonated species are also present in both samples [43], indicating that a fraction of strong Brønsted acid sites are located where collidine can access them (i.e. at the external surface and/or in the vicinity of the pore mouths).

The analytical *19b* vibrational modes of pyridine adsorbed on strong Brønsted (band at 1545 cm^{-1}) and Lewis (band at 1455 cm^{-1}) acid sites are usually employed to obtain quantitative information about the aforementioned species [38]. By using one of the sets of molar extinction coefficients available in the literature for these vibrational modes[39] and the procedure describe in the experimental section, the results reported in Table 2 can be obtained.

The quantitative results derived from pyridine adsorption clearly indicate that the material synthesized following the fluoride route possesses a definitely higher concentration of Brønsted acid sites with respect to the materials obtained by the conventional synthesis at high pH. Moreover, both materials contain a fraction of strong Lewis acid sites due probably to the presence of some extra-framework Al species. The concentration of these last species is certainly higher in the case of the ZSM-5(OH) sample.

Table 2. Concentrations of Brønsted and strong Lewis acid sites in μmol/g determined by in situ IR spectroscopy of adsorbed pyridine after 2 h of outgassing at 473 K.

Sample	Lewis acid sites[a] (μmol/g)	Brønsted acid sites[b] (μmol/g)	Total acid sites (μmol/g)
ZSM-5(F)	26	395	411
ZSM-5(OH)	60	221	281

[a] Calculated evaluating the integrated area of the analytical 19b mode of Py at 1455 cm^{-1} 9 (in the dotted spectra of figure 7b) and the integrated molar extinction coefficient reported in ref. [39] by means of equation (2) .

[b] Calculated evaluating the integrated area of the analytical 19b mode of Py at 1545 cm^{-1} (in the dotted spectra of figure 7b) and the integrated molar extinction coefficient reported in ref. [39] by means of equation (1).

Further information about the actual location of the weak acidic SiOH groups can be obtained by collidine adsorption spectra, following the procedure reported in a recent paper by Signorile et al. [51]. The spectra of the two materials were reported, in the spectral region of unperturbed (isolated) and weakly perturbed (terminals) hydroxyl groups, in a band-resolved form considering three main spectral components (see Figure 7), after activation (upper part) and contact with collidine vapors (lower part). The three resolved components, hereafter referred to as I, II and III, are located at 3746, 3738 and 3723 cm^{-1} respectively. On the basis of the abundant literature about this topic [18,43], the signal at 3746 cm^{-1} can be ascribed to fully isolated (unperturbed) SiOH groups, whereas the two components at 3738 (II) and 3723 (III) cm^{-1} are generated by substantially unperturbed hydroxyls groups in terminal position in the hydrogen-bonded silanol chains generated by zeolite defects.

The integrated absorbances (A_{int}) of the various spectral components after activation and after contact with collidine vapors are reported in Table 3. In this particular case, a simple assessment of the location of the different OH families in the two samples has been carried out, without the requirement of absolute quantitative data. For this reason, the simple evaluation and comparison of the integrated areas of the different spectral components in the two materials was sufficient to obtain the desired information.

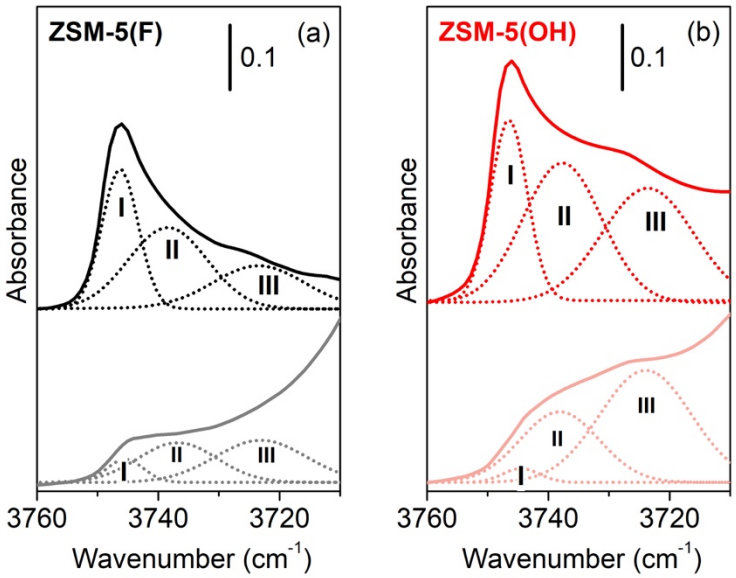

Figure 7. Band resolved IR spectra in the stretching region of substantially unperturbed OH species of ZSM-5(F) (section (a)) and ZSM-5(OH) (section (b)), normalized to the zeolite overtone modes, of the catalysts activated at 500°C (upper part: black-ZSM-5(F) and red-ZSM-5(OH)) and after contact with collidine vapor pressure (lower part: light grey-ZSM-5(F) and light red-ZSM-5(OH)). Full line spectra are the experimental ones, whereas dotted traces represent the resolved components, referred to as I, II and III.

It is evident that the ZSM-5(OH) sample contains an overall higher amount of weak acidic SiOH species. Moreover, by evaluating the integrated absorbances relative to the terminals SiOH groups virtually unaffected by collidine adsorption (i.e. actually located in the silicon vacancies present inside the micropores), the same material is characterized by a higher number of internal terminal hydroxyl. Finally, even if the external surface is characterized by the presence of basically only isolated SiOH species (as expected), both the zeolites contain a not negligible fraction of external terminal SiOH groups as well.

Table 3. Integrated absorbances (A_{int}) of the resolved spectral components I, II and III reported in Figure 8 evaluated after activation (internal + external SiOH fraction) and after contact with collidine vapors (internal SiOH fraction), relative to the isolated OH species (I) and to the total terminal (II+III) OH groups. The external SiOH fraction, calculated by difference, is reported for completeness.

Sample	Silanol location	A_{int} (I) Isolated	A_{int} (II + III) Terminals
ZSM-5(F) (activated)	Internal+external	1.76	3.58
ZSM-5(OH) (activated)	Internal+external	2.29	7.43
ZSM-5(F) (collidine)	Internal	0.29	2.42
ZSM-5(OH) (collidine)	Internal	0.18	5.49
ZSM-5(F) (difference)	External	1.47	1.16
ZSM-5(OH) (difference)	External	2.10	1.94

3.2 Catalytic evaluation

The careful IR characterization highlighted important differences between the materials synthetized following different routes. Indeed, the quantitative results derived from pyridine adsorption proved that the sample prepared using the fluoride medium possesses a definitely higher population of acid sites and, in particular, a higher concentration of bridging strongly acidic Al(OH)Si Brønsted species with respect to the materials obtained by the conventional route. In parallel, the IR data obtained by the adsorption of a more hindered molecular probe (collidine), proved that the ZSM-5(F) sample possesses a lower amount of terminals hydroxyl groups, correlated with the presence of silicon vacancies inside the micropores of the zeolite. The definitely lower population of these species proves that the material obtained through the fluoride route is characterized by a very low concentration of internal defects. Now, considering the different features of the two materials both in terms of amount

of strong acidic sites and of internal structural defects, it is possible to critically evaluate the following catalytic results.

Methanol conversions as a function of time on stream at a WHSV of 2 $g_{methanol}$ $g^{-1}_{catalyst}$ h^{-1} are shown for samples of ZSM-5(F) and ZSM-5(OH) in Figure 8a. Both samples display high initial methanol conversion, above 90% in the first reaction hours. During the first 24 hours, the methanol conversion of the ZSM-5(OH) catalyst is stable at ca 95%, while the ZSM-5(F) one stabilizes at a slightly lower value around 90%. However, after the 24 hours of time on stream, the conversion for the ZSM-5(OH) sample decreases, dropping from 95% to 66% during the next 40 hours. On the contrary, the ZSM-5(F) sample continues to exhibit the same high conversion level for as long as ca 145 h time on stream, when the conversion finally drops from 87 % to 60 % in further 20 h. The time up to deactivation onset is approximately 6 times longer in the case of ZSM-5(F) than for ZSM-5(OH), inferring a significant difference in the deactivation process for the two catalysts.

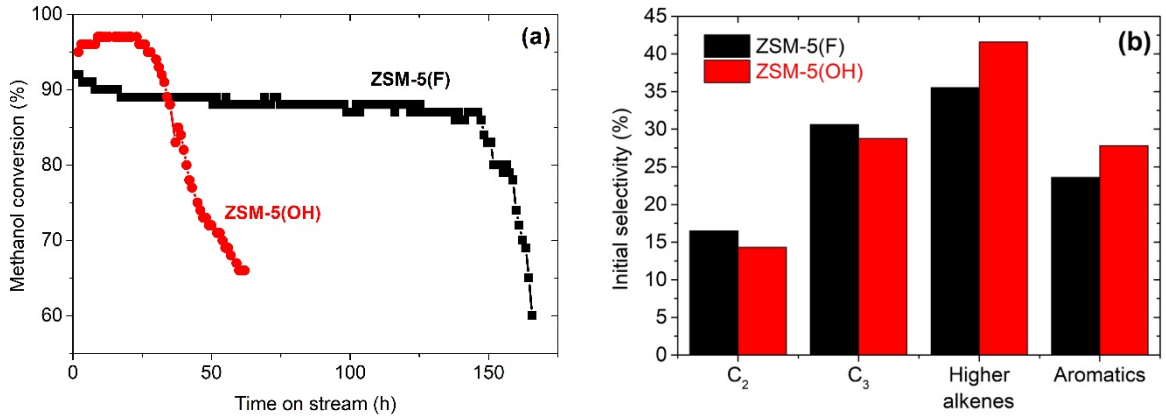

Figure 8. (a) methanol conversion as function of time on stream; and (b) initial products selectivity at a WHSV of 2 $g_{methanol}$ $g^{-1}_{catalyst}$ h^{-1} for the ZSM-5(F) (black) and ZSM-5(OH) (red) catalysts.

The longer lifetime in MTH for the ZSM-5(F) sample compared to ZSM-5(OH) observed here is in line with the previous report by Qin et al. [32]: nevertheless, the initial activity of ZSM-5(F) is in the range 90-95 %, which is higher than the initial activity of 200 nm thick ZSM-5(F) reported in the Qin paper (80%). The two samples are morphologically very similar, thus a comparable catalytic behavior would have been expected on the basis of this parameter only. Also the different concentration of acid sites could not be the main reason for slower deactivation in ZSM-5(F), since its higher amount of Brønsted sites (see Table 2) should enhance the deactivation according to the literature [47,48]. Furthermore, the similar strength of the acid sites as inferred by CO adsorption again points out as the acidity of the materials is not the primary cause determining the different deactivation processes in the two samples. The most remarkable parameter is indeed the different population of internal defects. This assumption is in agreement with the findings of Barbera et al., showing as a low density of internal structural defects delays deactivation in MTH catalysts [17]. Also Qin et al.[32] suggested that

deactivation occurs faster in crystals with higher density of internal defects, as these internal defects could be sufficiently large to accommodate easier highly methylated benzene species. These would then completely fill the nearby channel or intersection, thereby hindering other molecules from entering or passing the blocked domain, i.e. causing a molecular coke based deactivation process. The initial product selectivity (i.e. measured at early reaction stages, when conversion is maximum), reported in Figure 8b, is similar for both catalysts. As the selectivity is highly dependent on the size of the crystals [52,53], a similar behavior is expected due to the similar crystal size of catalysts presented in this work.

A further confirmation of such hypothesis arose from UV-Raman spectroscopy of the spent catalysts: this non-destructive technique has been proved to be an excellent tool in the characterization of deactivated MTH catalysts, since its superior sensitivity to both molecular and extended coke species [54–57]. The key advantages of UV-Raman with respect to conventional Raman (i.e. exploiting visible excitation light) are: i) the avoidance of photoluminescence phenomena (i.e. fluorescence) typical of coke moieties that hampers the collection of the Raman signal; and ii) the selective resonance of specific coke components whose electronic transitions fall in the UV region, such as polycyclic aromatic hydrocarbons (PAHs), thus achieving a superior sensitivity toward these species [58,59]. The results of the UV-Raman characterization performed over the spent ZSM-5(F) and ZSM-5(OH) catalysts are reported in Figure 9.

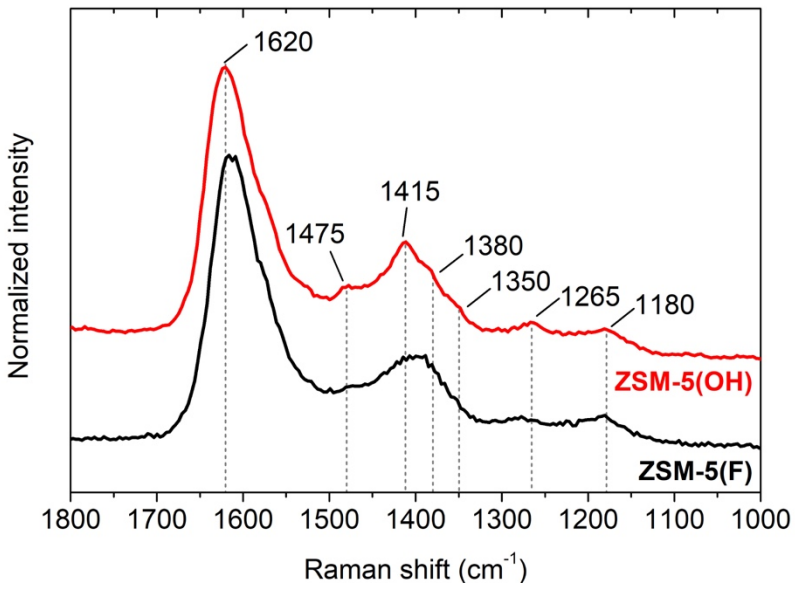

Figure 9. UV-Raman (244 nm) spectra of spent ZSM-5(F) (black) and ZSM-5(OH) (red) catalysts. Labels and vertical lines highlight the main spectral features ascribed to coke species.

The UV-Raman spectra of the deactivated ZSM-5 samples exhibit clear differences due to the different type of deactivating coke present in the two spent catalysts. In particular, the spectrum of ZSM-5(OH) shows much more pronounced spectral features with respect to the one of ZSM-5(F),

characterized instead by much broader signals. This outcome suggests the presence of a relevant fraction of molecular coke species in the case of ZSM-5(OH), giving rise to sharper vibrational signals. In detail, the bands at 1475 cm^{-1}, 1380 cm^{-1} and 1350 cm^{-1} are assigned to small PAHs (fluorene, naphthalene and phenantrene respectively), which also shows additional signals at around 1630 cm^{-1} [60]. The latter cannot be straightforwardly identified because they overlap with the intense G band of amorphous carbon (i.e. the bulk coke deposited at the external surface of the particles), generated by the stretching modes of pairs of sp^2 C atoms in rings and chains, giving rise to a broad band roughly centered at 1600 cm^{-1} [61,62]. The upward shift of the maximum at ca 1620 cm^{-1} can be ascribed to the superimposition of the G band with the PAHs signals located at slightly higher frequencies. Another relevant feature is the intense peak centered at 1415 cm^{-1}, that can be related to small PAHs in their methylated form [56]. The assignment is confirmed by the concurrent presence of a secondary peak of methyl-PAHs at 1180 cm^{-1}. Finally, the presence of some methylbenzenes (MBs) generate a peak at 1265 cm^{-1}: this specific feature exactly relates to 1,2,4,5-tetramethylbenzene, however other MBs with higher methylation (e.g. hexamethylbenzene) show intense signals nearby. In the case of ZSM-5(F), the Raman spectrum is much less defined and two main broad features are observed at ca 1600 cm^{-1} and 1400 cm^{-1}: the former is ascribed to the aforementioned G band of amorphous carbon, whereas the second is related to the breathing modes of the aromatic ring in an extended carbon phase, generally labeled as D band. No clear evidences of the presence of relevant amounts of molecular coke are found, excluding some small modulations in the spectrum at low frequencies compatible with the presence of methylated aromatic species. These findings suggest as in ZSM-5(F) the deactivation occurs due to the deposition of an external layer of bulk coke or small carbon species inside pore channels, whereas in ZSM-5(OH) some molecular coke (hosted in the wider cavities generated by internal defects) take part to the deactivation process.

Figure 10 schematically illustrates the coke formation process on MFI catalysts in presence/absence of internal defects on the basis of the observations presented in this work.

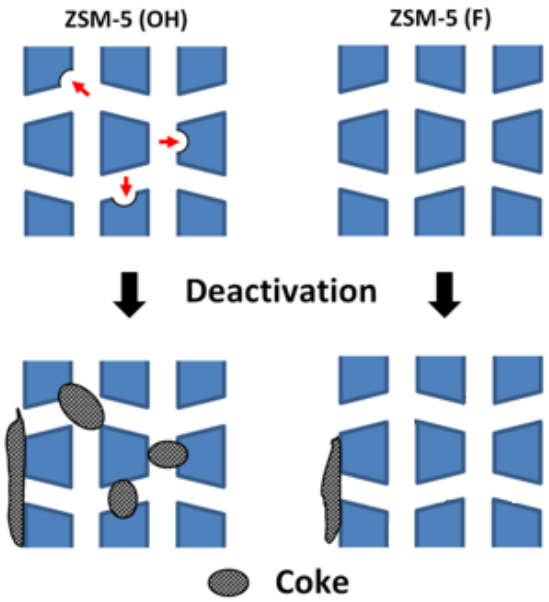

Figure 10. Schematic drawing of pristine frameworks with (top left) and without (top right) internal defects (labeled by red arrows), and corresponding frameworks after coke deposition (lower panes).

The top part of the figure shows the native frameworks with (left) and without defects (right), i.e. ideally ZSM-5(F) and ZSM-5(OH) respectively. The bottom part of the figure shows the same frameworks after accumulation of coke. As illustrated by the figure, the internal defects lead to formation of internal coke, of molecular nature as confirmed by UV-Raman results. The internal coke accumulation results in longer diffusion paths for the reactants/products and in the progressive decreased of catalyst activity. If the density of internal defect sites is sufficiently high, the pore system may eventually become almost completely inaccessible by percolation effects as coke is deposited. Under the assumption that there is one site in each channel segment and one in each intersection, the percolation threshold, expressed as the relative occupancy of the sites, for the MFI pore system is as low as 0.36 [63]. This means that when 36% of the sites are occupied, the transport through the pores is terminated. If, on the other hand, coke formation only occurs in the intersections, the blocking effect may be even more dramatic. In a previous work, we showed that the transport of helium through a zeolite MFI membrane was dramatically decreased several orders of magnitude when ca 20 % of the intersections were occupied by benzene molecules, the experimental observations were well described with a site percolation model with one site in each intersection [64]. Thus, coke occupying only a minor fraction of the intersections may potentially drastically reduce the diffusion rates of reactants and products in the pores and thereby reduce the performance of the catalyst. Moreover, Chen et al.[65] developed a percolation based model for describing the deactivation of a SAPO-34 catalyst for methanol conversion hydrocarbons, a system similar to the one studied in the present work. They found that the deactivation of the catalyst was well described by a percolation model.

4. Conclusions

ZSM-5 nanocrystalline samples were synthesized using both the fluoride route and conventional synthesis at high pH in an alkaline medium. The samples were carefully characterized by SEM, XRD, ICP-MS, IR spectroscopy, UV-Raman and N_2 adsorption at 77 K. The samples are very similar as regarding crystal size, morphology, specific surface area, acid sites strength, while slightly differs in the total amount of acid sites according to their different Si/Al ratio. The catalytic tests revealed that the sample prepared in fluoride medium shows a significantly longer lifetime compared to crystal prepared in hydroxyl medium. The faster deactivation of the samples synthesized in traditional hydroxyl medium was ascribed to accumulation of molecular coke species at the internal defect sites present in this sample, much more abundant in this material with respect to the fluoride-based one. The internal coke leads to reduced diffusion and percolation effects in the channel system, and this result in faster deactivation of larger crystals. In crystals prepared in fluoride medium, deactivation is probably mostly caused by deposition of an external layer of bulk coke. In summary, the results show that small crystals prepared using the fluoride route, thus minimizing the amount of internal structural defects, display high resistance towards deactivation by coke formation.

Acknowledgements

The authors would like to acknowledge the Swedish Energy Agency (Project numbers: 38028-1 and P41164-1), the Swedish Research Council (VR) and the ÅForsk foundation (ref. nr. 13-384) for financial support of this work. MS and VC acknowledge the Open Access Labs project for funding (2013–2015 agreement of Compagnia di San Paolo and Università di Torino). We thank Prof. Silvia Bordiga (University of Turin) for fruitful discussions.

References

[1] M. Stöcker, Methanol-to-hydrocarbons: catalytic materials and their behavior, Microporous Mesoporous Mater. 29 (1999) 3–48. doi:10.1016/S1387-1811(98)00319-9.

[2] F.J. Keil, Methanol-to-hydrocarbons: Process technology, Microporous Mesoporous Mater. 29 (1999) 49–66. doi:10.1016/S1387-1811(98)00320-5.

[3] J. Cobb, New Zealand Synfuel The Story of the World's First Natural Gas to Gasoline Plant, New Zealand Synthetic Fuels Corporation, 1985.

[4] http://www.topsoe.com/news/2014/08/groundbreaking-turkmenistan-build-major-plant-

producing-synthetic-gasoline, (n.d.). http://www.topsoe.com/news/2014/08/groundbreaking-turkmenistan-build-major-plant-producing-synthetic-gasoline.

[5] M. Bjorgen, S. Svelle, F. Joensen, J. Nerlov, S. Kolboe, F. Bonino, L. Palumbo, S. Bordiga, U. Olsbye, Conversion of methanol to hydrocarbons over zeolite H-ZSM-5: On the origin of the olefinic species, J. Catal. 249 (2007) 195–207. doi:10.1016/j.jcat.2007.04.006.

[6] H. Schulz, "Coking" of zeolites during methanol conversion: Basic reactions of the MTO-, MTP- and MTG processes, Catal. Today. 154 (2010) 183–194. doi:10.1016/j.cattod.2010.05.012.

[7] D.M. Bibby, R.F. Howe, G.D. McLellan, Coke formation in high-silica zeolites, Appl. Catal. A, Gen. 93 (1992) 1–34. doi:10.1016/0926-860X(92)80291-J.

[8] S. Müller, Y. Liu, M. Vishnuvarthan, X. Sun, A.C. Van Veen, G.L. Haller, M. Sanchez-Sanchez, J.A. Lercher, Coke formation and deactivation pathways on H-ZSM-5 in the conversion of methanol to olefins, J. Catal. 325 (2015) 48–59. doi:10.1016/j.jcat.2015.02.013.

[9] F. Schmidt, M.R. Lohe, B. Büchner, F. Giordanino, F. Bonino, S. Kaskel, Improved catalytic performance of hierarchical ZSM-5 synthesized by desilication with surfactants, Microporous Mesoporous Mater. 165 (2013) 148–157. doi:10.1016/j.micromeso.2012.07.045.

[10] U. Olsbye, S. Svelle, M. Bjørgen, P. Beato, T.V.W. Janssens, F. Joensen, S. Bordiga, K.P. Lillerud, Conversion of Methanol to Hydrocarbons: How Zeolite Cavity and Pore Size Controls Product Selectivity, Angew. Chem. Int. Ed. 51 (2012) 5810–5831. doi:10.1002/anie.201103657.

[11] J. Pérez-Ramírez, C.H. Christensen, K. Egeblad, C.H. Christensen, J.C. Groen, Hierarchical zeolites: enhanced utilisation of microporous crystals in catalysis by advances in materials design, Chem. Soc. Rev. 37 (2008) 2530. doi:10.1039/b809030k.

[12] K. Na, C. Jo, J. Kim, K. Cho, J. Jung, Y. Seo, R.J. Messinger, B.F. Chmelka, R. Ryoo, Directing Zeolite Structures into Hierarchically Nanoporous Architectures, Science (80-.). 333 (2011) 328–332. doi:10.1126/science.1204452.

[13] M. Choi, K. Na, J. Kim, Y. Sakamoto, O. Terasaki, R. Ryoo, Stable single-unit-cell nanosheets of zeolite MFI as active and long-lived catalysts, Nature. 461 (2009) 246–249.

doi:10.1038/nature08288.

[14] S. van Donk, A.H. Janssen, J.H. Bitter, K.P. de Jong, Generation, Characterization, and Impact of Mesopores in Zeolite Catalysts, Catal. Rev. 45 (2003) 297–319. doi:10.1081/CR-120023908.

[15] K. Kim, R. Ryoo, H.-D. Jang, M. Choi, Spatial distribution, strength, and dealumination behavior of acid sites in nanocrystalline MFI zeolites and their catalytic consequences, J. Catal. 288 (2012) 115–123. doi:10.1016/J.JCAT.2012.01.009.

[16] C. Mei, P. Wen, Z. Liu, H. Liu, Y. Wang, W. Yang, Z. Xie, W. Hua, Z. Gao, Selective production of propylene from methanol: Mesoporosity development in high silica HZSM-5, J. Catal. 258 (2008) 243–249. doi:10.1016/J.JCAT.2008.06.019.

[17] M. Ogura, S. Shinomiya, J. Tateno, Y. Nara, M. Nomura, E. Kikuchi, M. Matsukata, Alkali-treatment technique — new method for modification of structural and acid-catalytic properties of ZSM-5 zeolites, Appl. Catal. A Gen. 219 (2001) 33–43. doi:10.1016/S0926-860X(01)00645-7.

[18] M. Bjørgen, F. Joensen, M. Spangsberg Holm, U. Olsbye, K.-P. Lillerud, S. Svelle, Methanol to gasoline over zeolite H-ZSM-5: Improved catalyst performance by treatment with NaOH, Appl. Catal. A Gen. 345 (2008) 43–50. doi:10.1016/J.APCATA.2008.04.020.

[19] M. Zhou, A.A. Rownaghi, J. Hedlund, Synthesis of mesoporous ZSM-5 zeolite crystals by conventional hydrothermal treatment, RSC Adv. 3 (2013) 15596. doi:10.1039/c3ra42199f.

[20] A.A. Rownaghi, J. Hedlund, Methanol to Gasoline-Range Hydrocarbons: Influence of Nanocrystal Size and Mesoporosity on Catalytic Performance and Product Distribution of ZSM-5, Ind. Eng. Chem. Res. 50 (2011) 11872–11878. doi:10.1021/ie201549j.

[21] M.A. Camblor, L.A. Villaescusa, M.J. Díaz- Cabañas, Synthesis of all-silica and high-silica molecular sieves in fluoride media, Top. Catal. 9 (1999) 59–76. doi:10.1023/A:1019154304344.

[22] M. Zhou, J. Hedlund, Facile Preparation of Hydrophobic Colloidal MFI and CHA Crystals and Oriented Ultrathin Films, Angew. Chem. Int. Ed. 57 (2018) 10966–10970. doi:10.1002/anie.201806502.

[23] M.A. Camblor, A. Corma, S. Valencia, Spontaneous nucleation and growth of pure silica zeolite-Beta free of connectivity defects, Chem. Commun. 0 (1996) 2365–2366. doi:10.1039/cc9960002365.

[24] F. Thibault-Starzyk, A. Vimont, C. Fernandez, J.-P. Gilson, 2D correlation IR spectroscopy of xylene isomerisation on H-MFI zeolite, Chem. Commun. (2000) 1003–1004. doi:10.1039/b002007i.

[25] F. Thibault-Starzyk, A. Vimont, J.-P. Gilson, 2D-COS IR study of coking in xylene isomerisation on H-MFI zeolite, Catal. Today. 70 (2001) 227–241. doi:10.1016/S0920-5861(01)00420-5.

[26] P. Sazama, B. Wichterlova, J. Dedecek, Z. Tvaruzkova, Z. Musilova, L. Palumbo, S. Sklenak, O. Gonsiorova, FTIR and 27Al MAS NMR analysis of the effect of framework Al- and Si-defects in micro- and micro-mesoporous H-ZSM-5 on conversion of methanol to hydrocarbons, Microporous Mesoporous Mater. 143 (2011) 87–96. doi:10.1016/J.MICROMESO.2011.02.013.

[27] K. Barbera, F. Bonino, S. Bordiga, T.V.W. Janssens, P. Beato, Structure-deactivation relationship for ZSM-5 catalysts governed by framework defects, J. Catal. 280 (2011). doi:10.1016/j.jcat.2011.03.016.

[28] I. Yarulina, J. Goetze, C. Gücüyener, L. van Thiel, A. Dikhtiarenko, J. Ruiz-Martinez, B.M. Weckhuysen, J. Gascon, F. Kapteijn, Methanol-to-olefins process over zeolite catalysts with DDR topology: effect of composition and structural defects on catalytic performance, Catal. Sci. Technol. 6 (2016) 2663–2678. doi:10.1039/C5CY02140E.

[29] S. Prodinger, M.A. Derewinski, A. Vjunov, S.D. Burton, I. Arslan, J.A. Lercher, Improving Stability of Zeolites in Aqueous Phase via Selective Removal of Structural Defects, J. Am. Chem. Soc. 138 (2016) 4408–4415. doi:10.1021/jacs.5b12785.

[30] J. Grand, S.N. Talapaneni, A. Vicente, C. Fernandez, E. DIb, H.A. Aleksandrov, G.N. Vayssilov, R. Retoux, P. Boullay, J.P. Gilson, V. Valtchev, S. Mintova, One-pot synthesis of silanol-free nanosized MFI zeolite, Nat. Mater. 16 (2017) 1010–1015. doi:10.1038/nmat4941.

[31] J. Grand, S.N. Talapaneni, H.A. Aleksandrov, G.N. Vayssilov, S. Mintova, Hydrophobic

Tungsten-Containing MFI-Type Zeolite Films for Exhaust Gas Detection, ACS Appl. Mater. Interfaces. 11 (2019) 12914–12919. doi:10.1021/acsami.8b17626.

[32] J.M. Chezeau, L. Delmotte, J.L. Guth, Z. Gabelica, Influence of synthesis conditions and postsynthesis treatments on the nature and quantity of structural defects in highly siliceous MFI zeolites: A high-resolution solid-state 29Si n.m.r. study, Zeolites. 11 (1991) 598–606. doi:10.1016/S0144-2449(05)80011-9.

[33] F.C. Meunier, D. Verboekend, J.-P. Gilson, J.C. Groen, J. Pérez-Ramírez, Influence of crystal size and probe molecule on diffusion in hierarchical ZSM-5 zeolites prepared by desilication, Microporous Mesoporous Mater. 148 (2012) 115–121. doi:10.1016/J.MICROMESO.2011.08.002.

[34] S. Ivanova, C. Lebrun, E. Vanhaecke, C. Pham-Huu, B. Louis, Influence of the zeolite synthesis route on its catalytic properties in the methanol to olefin reaction, J. Catal. 265 (2009) 1–7. doi:10.1016/J.JCAT.2009.03.016.

[35] F.L. Bleken, S. Chavan, U. Olsbye, M. Boltz, F. Ocampo, B. Louis, Conversion of methanol into light olefins over ZSM-5 zeolite: Strategy to enhance propene selectivity, Appl. Catal. A Gen. 447 (2012) 178–185. doi:10.1016/j.apcata.2012.09.025.

[36] Z. Qin, L. Lakiss, L. Tosheva, J.-P. Gilson, A. Vicente, C. Fernandez, V. Valtchev, Comparative Study of Nano-ZSM-5 Catalysts Synthesized in OH^- and F^- Media, Adv. Funct. Mater. 24 (2014) 257–264. doi:10.1002/adfm.201301541.

[37] V. Crocellà, T. Tabanelli, J.G. Vitillo, D. Costenaro, C. Bisio, F. Cavani, S. Bordiga, A multi-technique approach to disclose the reaction mechanism of dimethyl carbonate synthesis over amino-modified SBA-15 catalysts, Appl. Catal. B Environ. 211 (2017) 323–336. doi:10.1016/j.apcatb.2017.04.013.

[38] J.W. Harris, M.J. Cordon, J.R. Di Iorio, J.C. Vega-Vila, F.H. Ribeiro, R. Gounder, Titration and quantification of open and closed Lewis acid sites in Sn-Beta zeolites that catalyze glucose isomerization, J. Catal. 335 (2016) 141–154. doi:10.1016/j.jcat.2015.12.024.

[39] C.A. Emeis, Determination of Integrated Molar Extinction Coefficients for Infrared Absorption Bands of Pyridine Adsorbed on Solid Acid Catalysts, J. Catal. 141 (1993) 347–354.

doi:10.1006/JCAT.1993.1145.

[40] M. Signorile, F. Bonino, A. Damin, S. Bordiga, A Novel Raman Setup Based on Magnetic-Driven Rotation of Sample, Top. Catal. 61 (2018) 1491–1498. doi:10.1007/s11244-018-1033-z.

[41] H. van Koningsveld, J.C. Jansen, H. van Bekkum, The monoclinic framework structure of zeolite H-ZSM-5. Comparison with the orthorhombic framework of as-synthesized ZSM-5, Zeolites. 10 (1990) 235–242. doi:10.1016/0144-2449(94)90134-1.

[42] S.P. Mirajkar, A. Thangaraj, V.P. Shiralkar, Sorption properties of titanium silicate molecular sieves, J. Phys. Chem. 96 (1992) 3073–3079. doi:10.1021/j100186a055.

[43] M.S. Holm, S. Svelle, F. Joensen, P. Beato, C.H. Christensen, S. Bordiga, M. Bjorgen, Assessing the acid properties of desilicated ZSM-5 by FTIR using CO and 2,4,6-trimethylpyridine (collidine) as molecular probes, Appl. Catal. a-General. 356 (2009) 23–30. doi:10.1016/j.apcata.2008.11.033.

[44] T. Armaroli, A. Gutiérrez Alejandre, M. Bevilacqua, M. Trombetta, F. Milella, J. Ramírez, G. Busca, 13-P-25-FTIR studies of the interaction of aromatic and branched aliphatic compounds with internal, external and extraframework sites of MFI-type zeolite materials, Stud. Surf. Sci. Catal. 135 (2001) 346. doi:10.1016/S0167-2991(01)81804-8.

[45] H. V Brand, A. Redondo, P.J. Hay, Theoretical studies of CO adsorption on H-ZSM-5 and hydrothermally treated H-ZSM-5, J. Mol. Catal. a-Chemical. 121 (1997) 45–62. doi:10.1016/s1381-1169(96)00456-6.

[46] C. Pazé, S. Bordiga, C. Lamberti, M. Salvalaggio, A. Zecchina, G. Bellussi, Acidic Properties of H−β Zeolite As Probed by Bases with Proton Affinity in the 118−204 kcal mol -1 Range: A FTIR Investigation, J. Phys. Chem. B. 101 (1997) 4740–4751. doi:10.1021/jp970649z.

[47] A. Platon, W.J. Thomson, Low-temperature test reaction for hydride transfer on solid acid catalysts, Catal. Letters. 101 (2005) 15–20. doi:10.1007/s10562-005-3741-9.

[48] A. Zecchina, C. Otero Areán, G. Turnes Palomino, F. Geobaldo, C. Lamberti, G. Spoto, S. Bordiga, The vibrational spectroscopy of H2, N2, CO and NO adsorbed on the titanosilicate molecular sieve ETS-10, Phys. Chem. Chem. Phys. 1 (1999) 1649–1657.

doi:10.1039/a808741e.

[49] F. Wakabayashi, J.N. Kondo, K. Domen, C. Hirose, Direct Comparison of N2 and CO as IR-Spectroscopic Probes of Acid Sites in H-ZSM-5 Zeolite, J. Phys. Chem. 99 (1995) 10573–10580. doi:10.1021/j100026a021.

[50] C. Morterra, G. Cerrato, Titrating surface acidity of sulfated zirconia catalysts: is the adsorption of pyridine a suitable probe?, Phys. Chem. Chem. Phys. 1 (1999) 2825–2831. doi:10.1039/a902029b.

[51] M. Signorile, V. Crocellà, A. Damin, B. Rossi, C. Lamberti, F. Bonino, S. Bordiga, Effect of Ti Speciation on Catalytic Performance of TS-1 in the Hydrogen Peroxide to Propylene Oxide Reaction, J. Phys. Chem. C. 122 (2018) 9021–9034. doi:10.1021/acs.jpcc.8b01401.

[52] Y. Shen, T.T. Le, D. Fu, J.E. Schmidt, M. Filez, B.M. Weckhuysen, J.D. Rimer, Deconvoluting the Competing Effects of Zeolite Framework Topology and Diffusion Path Length on Methanol to Hydrocarbons Reaction, ACS Catal. 8 (2018) 11042–11053. doi:10.1021/acscatal.8b02274.

[53] F. Mohammadparast, R. Halladj, S. Askari, The Crystal Size Effect of Nano-Sized ZSM-5 in the Catalytic Performance of Petrochemical Processes: A Review, Chem. Eng. Commun. 202 (2015) 542–556. doi:10.1080/00986445.2014.952815.

[54] D. Rojo-Gama, M. Signorile, F. Bonino, S. Bordiga, U. Olsbye, K.P. Lillerud, P. Beato, S. Svelle, Structure–deactivation relationships in zeolites during the methanol–to-hydrocarbons reaction: Complementary assessments of the coke content, J. Catal. 351 (2017) 33–48. doi:10.1016/j.jcat.2017.04.015.

[55] H. An, F. Zhang, Z. Guan, X. Liu, F. Fan, C. Li, Investigating the Coke Formation Mechanism of H-ZSM-5 during Methanol Dehydration Using Operando UV–Raman Spectroscopy, ACS Catal. 8 (2018) 9207–9215. doi:10.1021/acscatal.8b00928.

[56] M. Signorile, D. Rojo-Gama, F. Bonino, P. Beato, S. Svelle, S. Bordiga, Topology-dependent hydrocarbon transformations in the methanol-to-hydrocarbons reaction studied by operando UV-Raman spectroscopy, Phys. Chem. Chem. Phys. 20 (2018) 26580–26590. doi:10.1039/C8CP04240C.

[57] M. Signorile, D. Rojo Gama, F. Bonino, S. Svelle, P. Beato, S. Bordiga, Operando UV-Raman study of the methanol to olefins reaction over SAPO-34: Spatiotemporal evolution monitored by different reactor approaches, Catal. Today. (2018). doi:10.1016/j.cattod.2018.11.065.

[58] S. Asher, C. Johnson, Raman spectroscopy of a coal liquid shows that fluorescence interference is minimized with ultraviolet excitation, Science (80-.). 225 (1984) 311–313. doi:10.1126/science.6740313.

[59] Y.T. Chua, P.C. Stair, An ultraviolet Raman spectroscopic study of coke formation in methanol to hydrocarbons conversion over zeolite H-MFI, J. Catal. 213 (2003) 39–46. doi:10.1016/s0021-9517(02)00026-x.

[60] M. Signorile, F. Bonino, A. Damin, S. Bordiga, In Situ Resonant UV-Raman Spectroscopy of Polycyclic Aromatic Hydrocarbons, J. Phys. Chem. C. 119 (2015) 11694–11698. doi:10.1021/acs.jpcc.5b02209.

[61] A.C. Ferrari, J. Robertson, Resonant Raman spectroscopy of disordered, amorphous, and diamondlike carbon, Phys. Rev. B. 64 (2001) 075414. doi:10.1103/PhysRevB.64.075414.

[62] a. Ferrari, J. Robertson, Interpretation of Raman spectra of disordered and amorphous carbon, Phys. Rev. B. 61 (2000) 14095–14107. doi:10.1103/PhysRevB.61.14095.

[63] B.L. Trout, A.K. Chakraborty, A.T. Bell, Diffusion and reaction in ZSM-5 studied by dynamic Monte Carlo, Chem. Eng. Sci. 52 (1997) 2265–2276. doi:10.1016/S0009-2509(97)00010-9.

[64] J. Hedlund, M. Grahn, D. Korelskiy, M. Rayson, S. Öberg, P.R. Briddon, Mass transport in porous media from first principles: An experimental and theoretical study, J. Memb. Sci. 415–416 (2012) 271–277. doi:10.1016/J.MEMSCI.2012.05.009.

[65] D. Chen, H.P. Rebo, A. Holmen, Diffusion and deactivation during methanol conversion over SAPO-34: a percolation approach, Chem. Eng. Sci. 54 (1999) 3465–3473. doi:10.1016/S0009-2509(98)00474-6.